The Astrophysical Journal, 587:171–185, 2003 April 10
© 2003. The American Astronomical Society. All rights reserved. Printed in U.S.A.

A ^{12}CO $J = 6$–5 MAP OF M82: THE SIGNIFICANCE OF WARM MOLECULAR GAS

John S. Ward[1] and Jonas Zmuidzinas
Department of Physics, 320-47, California Institute of Technology, Pasadena, CA 91125;
john.ward@jpl.nasa.gov, jonas@submm.caltech.edu

and

Andrew I. Harris and Kate G. Isaak[2]
Astronomy Department, University of Maryland, College Park, MD 20742;
harris@astro.umd.edu, isaak@mrao.cam.ac.uk
Received 2001 November 17; accepted 2002 December 23

ABSTRACT

We present a ^{12}CO $J = 6$–5 map of the nuclear regions of the starburst galaxy M82 at a resolution of 14″ taken at the Caltech Submillimeter Observatory (CSO). Hot spots were found on either side of the dynamical center. We compare our results with a high-resolution ^{12}CO $J = 2$–1 interferometer map, and present a ^{12}CO $J = 6$–5/^{12}CO $J = 2$–1 line ratio map obtained using a novel deconvolution technique. This line ratio is highest at the two $J = 6$–5 integrated intensity peaks, reaching 0.4 and 0.5 in the northeast and southwest peaks, respectively, and is typically 0.2 elsewhere in the nuclear region. We also present measurements of ^{12}CO $J = 4$–3, ^{12}CO $J = 3$–2, and ^{13}CO $J = 3$–2, and an upper limit for ^{13}CO $J = 6$–5. We analyze these observations in the context of a two-component large velocity gradient (LVG) excitation model. Likelihood density curves were calculated for each of the model parameters and a variety of related physical quantities for the northeast and southwest peaks based on the measured line intensities and their associated uncertainties. This approach reveals in an unbiased way how well various quantities can be constrained by the CO observations. We find that the beam-averaged ^{12}CO and ^{13}CO column densities, the isotopomer abundance ratio, and the area filling factors are among the best constrained quantities, while the cool component H_2 density and pressure are less well constrained. The results of this analysis suggest that the warm gas is less dense than the cool gas, and that over half of the total molecular gas mass in these nuclear regions is warmer than 50 K.

Subject headings: galaxies: individual (M82) — galaxies: ISM — galaxies: starburst — submillimeter

1. INTRODUCTION

M82, also known as NGC 3034, is a nearby irregular starburst galaxy in Ursa Major, and is seen nearly edge-on. Dust obscures the nuclear region at optical wavelengths. M82 is the brightest IR galaxy in the sky, and has a total IR luminosity of 3.8×10^{10} $L_\odot$ (Colbert et al. 1999). It is believed that the starburst was triggered by a close encounter with M81 about 10^8 yr ago (Yun, Ho, & Lo 1993). The bright far-infrared (FIR) fine-structure lines seen in the inner kiloparsec of M82 imply a far-UV radiation field about 10^3 times larger than the local solar value (Colbert et al. 1999). This strong UV field is generated by a population of massive young stars that also heat the dust which produces the large IR luminosity. The nucleus has a large molecular gas mass, a few $\times 10^8$ $M_\odot$, giving rise to strong CO emission (Wild et al. 1992; Weiss et al. 2001). At an estimated current star formation rate of 1 $M_\odot$ yr^{-1}, this gas will be consumed in about 2×10^8 yr (Lord et al. 1996). Maps of both molecular line emission and thermal dust continuum show a double-peaked structure in the central kiloparsec (Neininger et al. 1998; Hughes, Gear, & Robson 1994).

The CO $J = 6$–5 line was first detected toward M82 by Harris et al. (1991), who showed that molecular gas in starburst galaxies is substantially warmer than in typical disk clouds. The CO $J = 6$–5 transition probes higher excitation temperatures (116 K above the ground state) than the more accessible CO $J = 1$–0 (5.5 K), CO $J = 2$–1 (17 K), and CO $J = 3$–2 (33 K) transitions. The higher J spectral lines thus provide important information needed to understand the large mass of $T \sim 100$ K molecular gas that is heated by massive young stars in a starburst galaxy. Recent improvements in receiver technology now allow high-quality maps to be made of the ^{12}CO $J = 6$–5 and $J = 7$–6 rotational lines in nearby galaxies. Mao et al. (2000) recently mapped the ^{12}CO $J = 7$–6 line. We present here a map of ^{12}CO $J = 6$–5.

As improving receiver technology provides astronomers with ever higher quality data, advances in digital computers open up possibilities for analyzing observations in new and better ways. For instance, CO excitation analyses in the large velocity gradient (LVG) approximation can now be calculated in a few milliseconds on a typical modern desktop computer. This allows us to evaluate multicomponent models with many parameters, examining huge volumes of parameter space to find all combinations of the model parameters consistent with the measured data rather than only calculating some narrow range of possible solutions. Using measured line intensities, we have calculated likelihood density functions for each of the parameters of a two-component LVG model for the northeast and southwest CO emission peaks. We have also calculated likelihood functions for a variety of physical quantities derived from these parameters, such as the pressure and the beam-averaged column density. These likelihood curves were used to find median likelihood estimators and 95% confidence intervals for the quantities of interest.

We have also developed a novel deconvolution technique to compute line ratio maps when a high-quality,

[1] Current address: Mail Stop 168-314, Jet Propulsion Laboratory, 4800 Oak Grove Drive, Pasadena, CA 91109-8099.

[2] Current address: Cavendish Astrophysics, University of Cambridge, Cambridge CB3 0HE, UK.

high-resolution map is available for the denominator and both maps are of the same species. This technique uses all spatial and velocity information in both maps, and can calculate the line ratio at a higher spatial resolution than the numerator map. With this technique, information is not thrown away, as with the common method of integrating away the velocity information and smoothing the higher resolution map before dividing.

2. OBSERVATIONS

All observations were performed at the Caltech Submillimeter Observatory (CSO) in 1998 January and 1999 January using SIS receivers operating in double-sideband mode. The ^{12}CO $J = 6$–5 map was made in excellent weather ($\tau_{225\,\mathrm{GHz}} \lesssim 0.04$), with typical single-sideband system temperatures (including the atmosphere) around 3000 K. The receiver consisted of a quasi-optical SIS mixer with an integrated HEMT low noise amplifier (LNA); an upgraded version of this receiver was described by Ward et al. (2000). The use of a broadband tunerless receiver reduces calibration errors associated with receiver sideband imbalance. A pair of 1024 channel, 500 MHz acousto-optical spectrometers were used as back ends. The chopping secondary was switched at a 1 Hz rate with a 60″ throw in azimuth. Spectral intensities were calibrated on an ambient-temperature chopper wheel and the sky periodically during the observations. Beam maps of Saturn were used to determine the beam FWHP of approximately 14″, and the main beam efficiency of 30%.

We do not have information about the error beam, which would contain most of the missing power; as a result, we are using a conservative estimate of 30% for the total calibration uncertainty.

The map of M82 consists of 36 positions on 7″.5 centers, and covers 70″ along the major axis of the galaxy and 50″ along the minor axis (Fig. 1). At a distance of 3.6 Mpc (Freedman et al. 1994), this corresponds to an area of 1200×880 pc mapped with a 250 pc FWHP beam. The coordinates of the $J = 6$–5 map were corrected for systematic pointing offsets by comparing line velocity structure to ^{12}CO $J = 2$–1 and C^{18}O $J = 1$–0 Plateau de Bure Interferometer data cubes from Weiss et al. (2001), according to the following procedure. A line connecting the antenna temperature peaks of the bright hot spots on either side of the dynamical center was found. This line was then drawn on top of a contour map of line center velocity,

$$v_c = \frac{\int T_A v\, dv}{\int T_A\, dv} . \quad (1)$$

The contours of constant velocity crossed the line at nearly right angles. A reference point was chosen where the line connecting the hot spots crossed the 200 km s^{-1} velocity contour. The coordinates of the ^{12}CO $J = 6$–5 map were then adjusted to match the reference point to the coordinates of a point found the same way in the interferometer maps. The correction was 4″.5 in right ascension and 7″.2 in declination, for a total shift of about 0.6 of the FWHP beam. This shift may have arisen because the telescope fixed pointing offsets were not determined immediately preceding the observations. The total pointing uncertainty is about 4″ in each axis. Maps of integrated intensity and peak antenna temperature are shown in Figures 2 and 3, respectively. Position-velocity plots are shown in Figure 4.

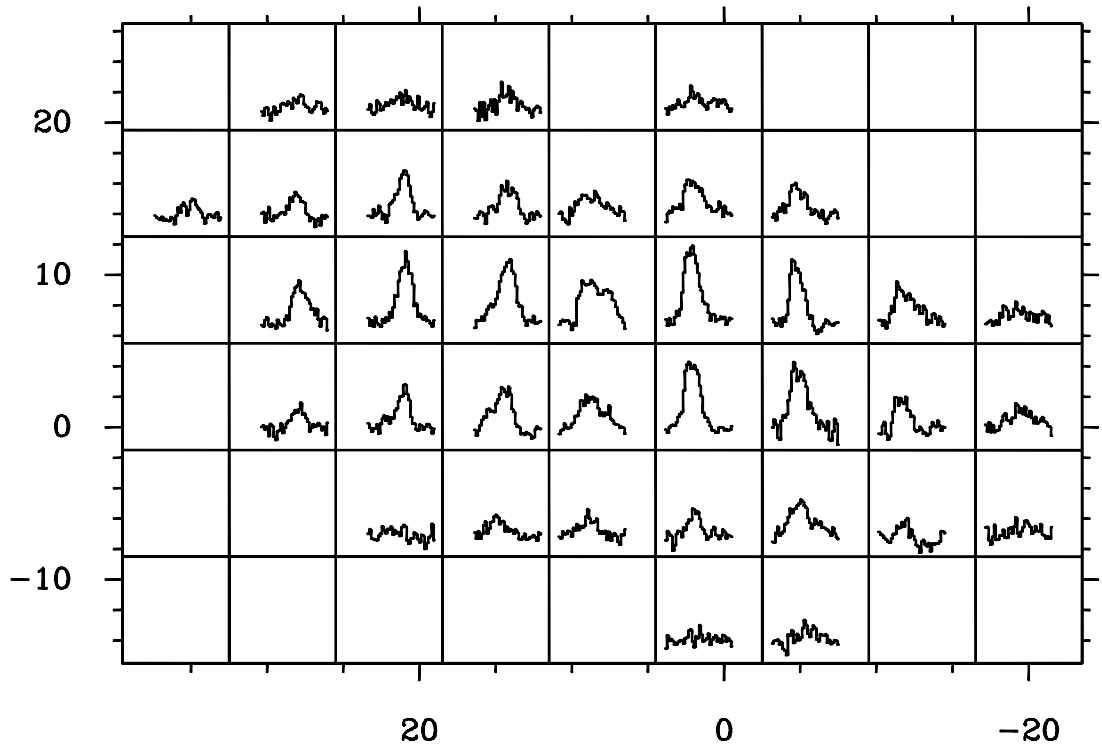

Fig. 1.—Spectra of ^{12}CO $J = 6$–5 in M82. The map has been rotated such that the horizontal offsets are approximately along the major axis. Offsets are in arcsec from an arbitrary center. The vertical scale ranges from T_{MB} of −1 to 4.5 K, and the horizontal scale ranges from −80 to 520 km s^{-1}.

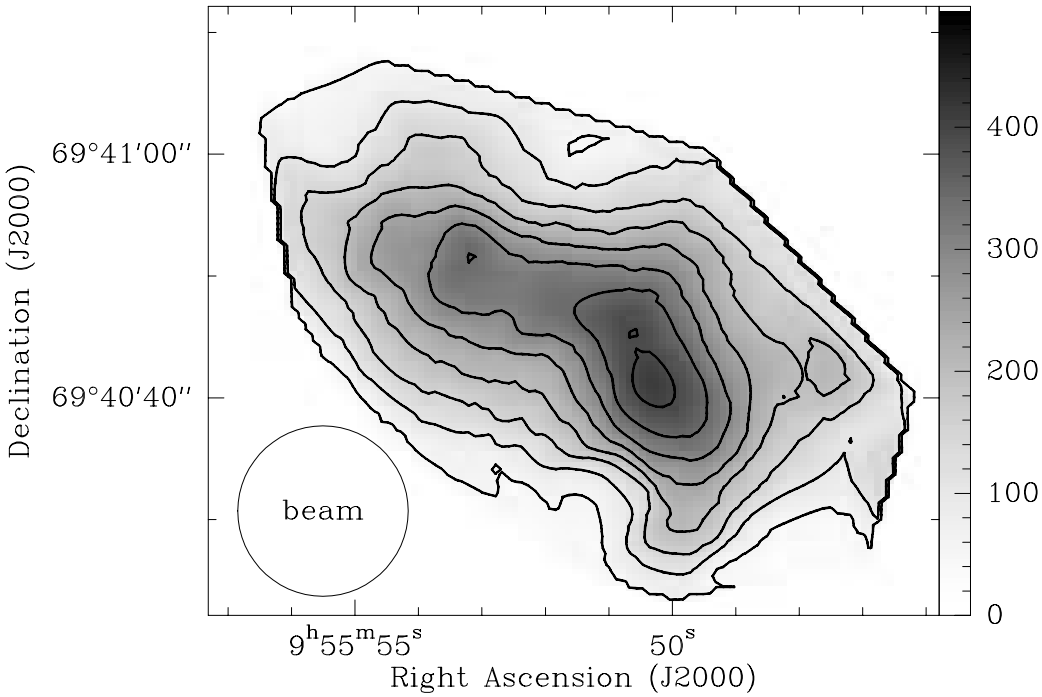

FIG. 2.—Integrated intensity of ^{12}CO $J = 6$–5 in M82. Contours are 50, 100, 150, 200, 250, 300, 350, and 400 K km s^{-1}.

In addition to the ^{12}CO $J = 6$–5 map, we have also observed 17 positions of the ^{12}CO $J = 4$–3 line, nine positions of ^{12}CO $J = 3$–2, and five positions of ^{13}CO $J = 3$–2, all with the CSO facility SIS receivers. Most of these positions were observed as cuts along the major axis of the galaxy. The beam sizes were 16″.5, 24″.4, and 25″.5 FWHP at 461, 346, and 331 GHz, respectively, with corresponding main beam efficiencies of 0.45, 0.50, and 0.50. The CO $J = 3$–2 observations were made with a 4 GHz wideband analog correlator spectrometer (WASP) similar to that described by Harris & Zmuidzinas (2001). The ^{13}CO $J = 3$–2 spectra were scaled up by 14% to account for the difference in atmospheric transmission in the two sidebands. We also integrated on the ^{13}CO $J = 6$–5 line for a single

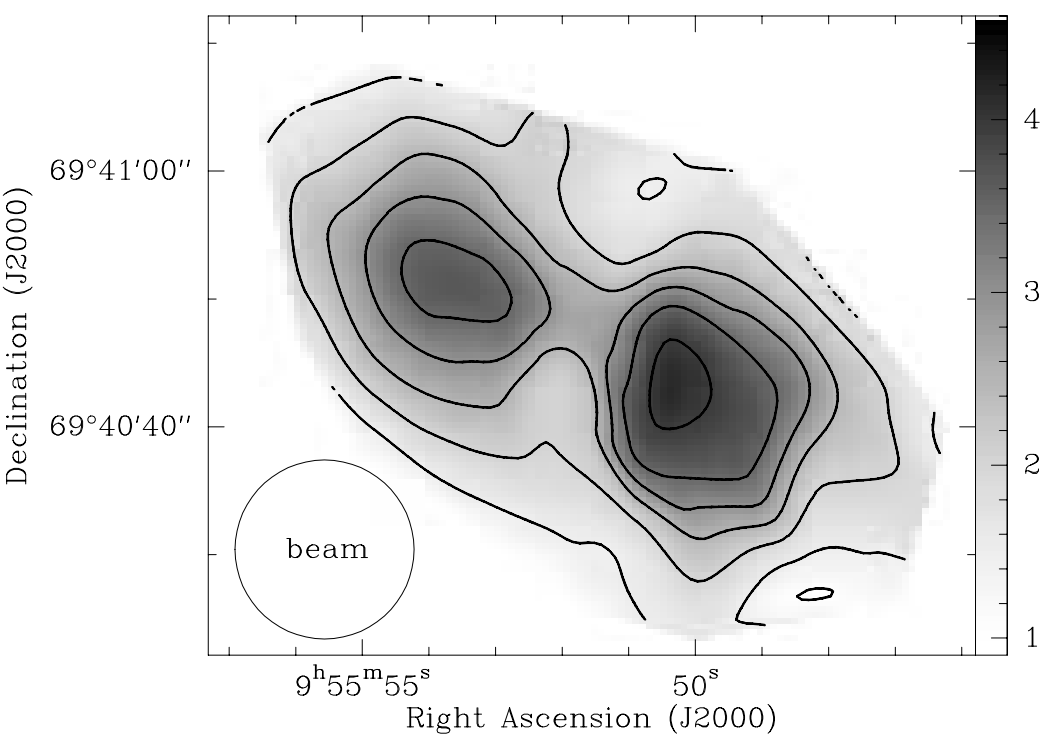

FIG. 3.—Peak antenna temperature of ^{12}CO $J = 6$–5 in M82. Contours are for T_{MB} of 1.0, 1.5, 2.0, 2.5, 3.0, 3.5, and 4.0 K.

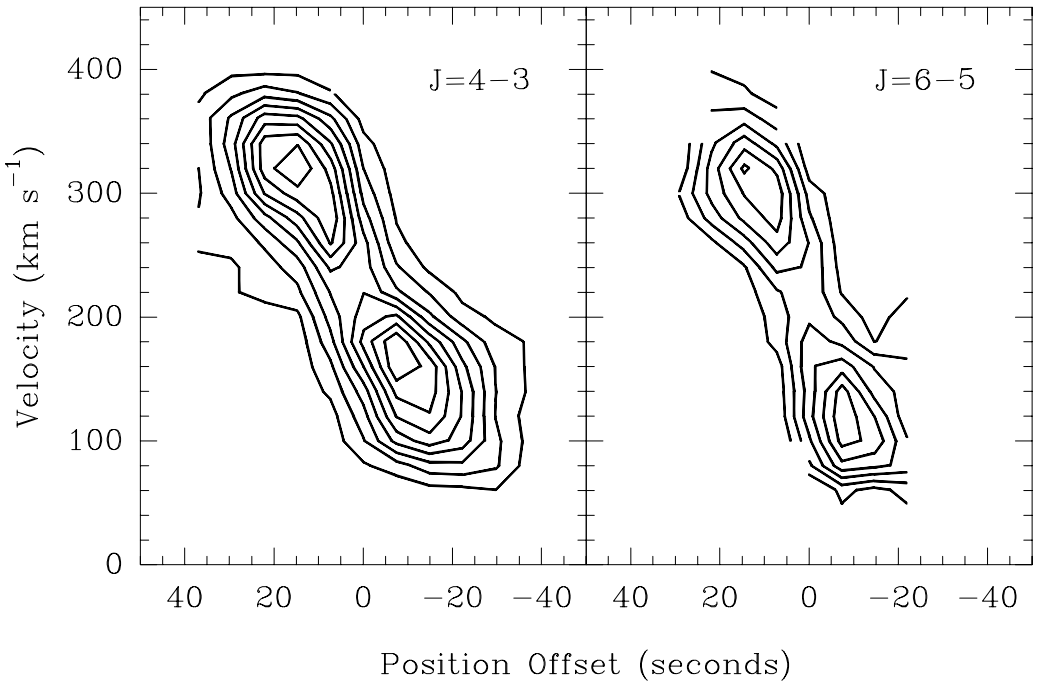

FIG. 4.—Position-velocity diagram along the major axis of M82 for ^{12}CO $J = 4$–3 and ^{12}CO $J = 6$–5. The southwest hot spot peaks at different velocities in the two transitions, and the overall velocity gradient is steeper in CO $J = 6$–5. Note that the broad, lower intensity spectrum between the two hot spots explains the difference in integrated intensity and peak temperature maps. The positions are offset from arbitrary centers along the major axis of the galaxy. Contours are for $T_{\rm MB}$ from 0.5 to 4 K in steps of 0.5 K.

pointing in 1998 January and 1999 January for a total of 96 minutes under conditions similar to those for the ^{12}CO $J = 6$–5 observations, but did not detect the line.

Zero-order baselines were subtracted from all reported measurements except ^{12}CO $J = 4$–3, which was corrected for a first-order baseline, and all reported results (including both the tables and the figures) are given on a main beam brightness temperature scale ($T_{\rm MB}$).

3. RESULTS

Figure 2 shows two peaks in integrated intensity, the southwest hot spot being stronger than the northeast. Comparing the integrated intensity to Figure 3, we see that the two hot spots are much more distinct in peak antenna temperature than in integrated intensity. This is due in part to a spatial smearing effect caused by the antenna beam width being comparable to the spacing between the hot spots, i.e., a 14″ FWHP beam compared to 19″ peak separation in Figure 3. The locations of the hot spots in the peak antenna temperature plot are less affected by smearing, since the hot spots differ in center velocity by 200 km s^{-1}.

Figure 5 shows the ^{12}CO $J = 6$–5 integrated intensity plotted over the ^{12}CO $J = 2$–1 map from Weiss et al. (2001). The hot spots in the CO $J = 6$–5 map are closer together than in the lower J map. This is consistent with the finding of Mao et al. (2000) that the angular separation of the lobes is smaller for a "high CO excitation component" than is seen in the low-J CO lines. It can be seen in the figure that the $J = 6$–5 southwest hot spot is located between the lower J southwest and center hot spots. This suggests that the southwest hot spot of the $J = 6$–5 map includes unresolved emission from both of these regions. The southwest hot spot appears to be somewhat extended in the direction of the minor axis in the $J = 6$–5 map. It is unlikely that this shape is real because it is not seen in any other published observations, including HCN $J = 1$–0 (Brouillet & Schilke 1993) and CO $J = 7$–6 (Mao et al. 2000) maps. It is also unlikely to be a calibration effect since the weather and receiver were very stable during the observations. It is possible that the telescope pointing drifted a few seconds of arc during the observations, causing this artifact.

The total luminosity of the ^{12}CO $J = 6$–5 line was found to be 9.0×10^5 $L_\odot$. This was calculated from the spatially and spectrally integrated intensity of 2.8×10^5 K km s^{-1} arcsec^2 after zeroth-order baseline subtraction, assuming spherically symmetric emission and a distance of 3.6 Mpc.

The ^{13}CO $J = 6$–5 line was not detected after 96 minutes of integration time near the central pointing. The 3 σ upper limit of the integrated intensity for a 14″ beam calculated from the rms channel noise is 7.9 K km s^{-1}. A reliable upper limit may be somewhat larger, however, since uncertainties in zeroth-order baseline subtraction and a small amount of baseline ripple could dominate over the channel noise. Nonetheless, with an implied $J = 6$–5 antenna temperature ratio of $I(^{12}{\rm CO})/I(^{13}{\rm CO}) \gtrsim 40$, it is clear that ^{13}CO $J = 6$–5 is very weak. Although ^{13}CO $J = 6$–5 emission was not detected, 450 μm continuum was observed at a level of 2.4 ± 0.6 Jy beam^{-1}. This is consistent with the bolometer value of 3.5 Jy beam^{-1} measured at the same location with a narrower 9″ FWHP beam by Hughes et al. (1994).

3.1. *A* ^{12}CO $J = 6$–5/^{12}CO $J = 2$–1 *Line Ratio Map*

Figure 6 shows a map of the ^{12}CO $J = 6$–5/^{12}CO $J = 2$–1 line ratio. The $J = 2$–1 data were observed with the Plateau de Bure Interferometer and include short-spacing corrections based on observations with the IRAM 30 m telescope (Weiss et al. 2001). The ratio map was calculated using a

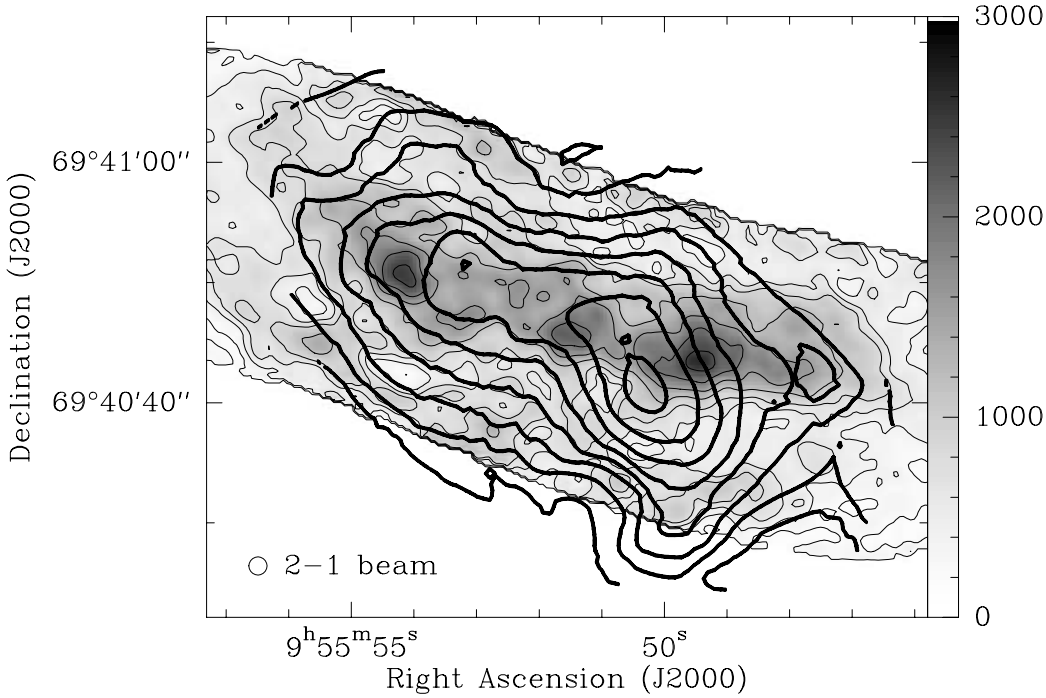

FIG. 5.—M82 ^{12}CO $J = 6$–5 integrated intensity contours superimposed on ^{12}CO $J = 2$–1 integrated intensity from Weiss et al. (2001). Contours are 50, 100, 150, 200, 250, 300, 350, and 400 K km s^{-1}.

novel deconvolution technique that takes advantage of velocity information in the $J = 6$–5 map along with the high spatial resolution of the $J = 2$–1 map to improve the resolution and accuracy of the ratio map. A Lagrange multiplier was used to set the relative weighting between minimizing the resulting χ^2 and maximizing the smoothness of the resulting ratio map. Details of the calculation are given in the Appendix. It is immediately apparent that the brightness temperature ratio is highest at the two integrated intensity peaks, reaching 0.4 and 0.5 in the northeast and southwest peaks, respectively, and is typically 0.2 elsewhere in the nuclear region.

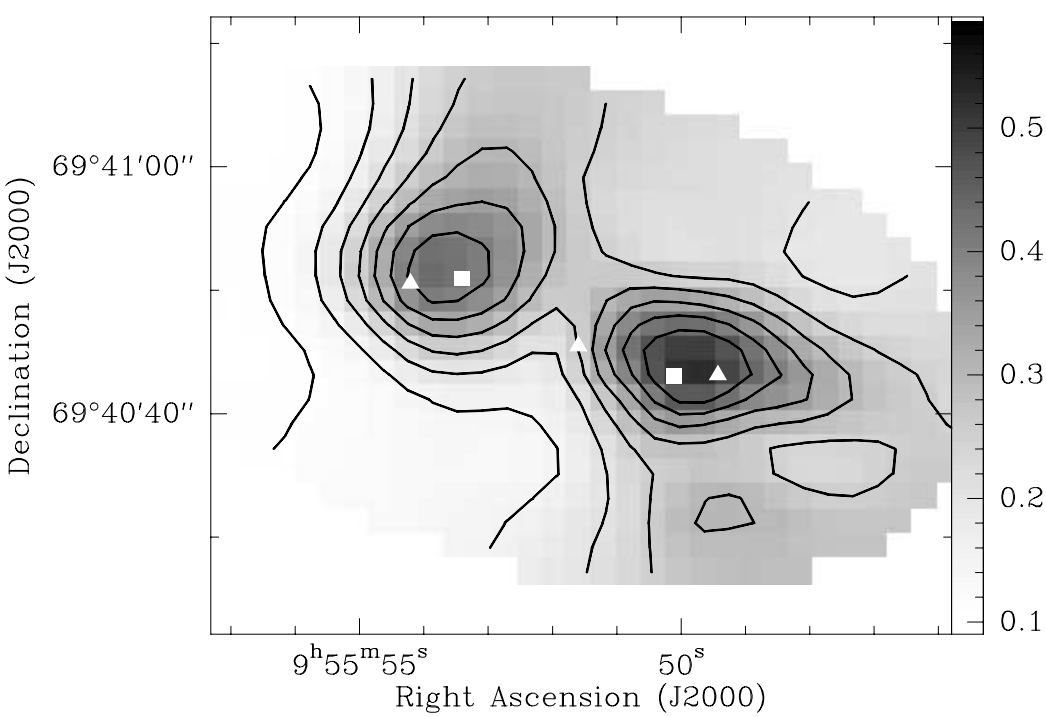

FIG. 6.—Deconvolved ^{12}CO $J = 6$–5/^{12}CO $J = 2$–1 brightness temperature ratio map. Contours are from 0.1 to 0.45 by 0.05. The squares indicate the locations of the $J = 6$–5 intensity peaks, and the triangles the locations of the $J = 2$–1 integrated intensity peaks.

TABLE 1
COBE Galactic Line Ratios

Location	$T_A(\mathrm{CO}\ J = 6\text{–}5)/T_A(\mathrm{CO}\ J = 2\text{–}1)$
Galactic center [a]	0.067 ± 0.010
Inner Galaxy [b]	<0.038
Outer Galaxy [c]	<0.10

Note.—Line ratios were calculated from measurements reported by Fixsen, Bennett, & Mather 1999. The uncertainty for the Galactic center ratio is 1 σ. Upper limits are 95% confidence. The beam width is 1° in Galactic latitude.
[a] Galactic longitude $|l| < 2\overset{\circ}{.}5$.
[b] Galactic longitude $2\overset{\circ}{.}5 < |l| < 32\overset{\circ}{.}5$.
[c] Galactic longitude $|l| > 32\overset{\circ}{.}5$.

3.2. *Comparisons to the Galactic Center*

It is informative to compare the nuclear region of M82 to the Galactic center. Both are seen nearly edge-on. The hot spots of M82 are each about 180 pc across, corresponding to $1\overset{\circ}{.}2$ at the Galactic center. With the exception of the circumnuclear disk (CND), the dust temperature over large scales in the Galactic center is a fairly uniform 21 K (Pierce-Price et al. 2000), compared to 48 K in the nuclear regions of M82 (Colbert et al. 1999; Hughes et al. 1994). The star formation rate in the central 500 pc of the Galaxy is about 0.3–0.6 $M_\odot$ yr^{-1} (Güsten 1989), compared to about 1 $M_\odot$ yr^{-1} in the central region of M82 (Lord et al. 1996).

Galactic CO emission up to $J = 8$–7 was measured with the *COBE* Far-Infrared Absolute Spectrophotometer (FIRAS). Line ratios calculated from measurements reported by Fixsen, Bennett, & Mather (1999) are presented in Table 1. Comparing this table to Figure 6, we see that the $J = 6$–5/$J = 2$–1 line ratio is at least 5 times larger in the southwest hot spot of M82 than in the Galactic center. It is clear that the proportion of molecular gas that is warm is significantly larger in the nuclear region of M82 than in the Galactic center.

3.3. *LVG Analysis*

Table 2 lists the inputs used in an excitation analysis of the two hot spots in M82. The analysis was performed using the LVG photon escape probability function $\beta = (1 - e^{-3\tau})/3\tau$ derived for plane-parallel clouds by Scoville & Solomon (1974). Results calculated with the escape probability function for spherical clouds in gravitational collapse $\beta = (1 - e^{-\tau})/\tau$ (Goldreich & Kwan 1974) differ in detail but do not change the basic results of this paper. Collision rate constants for excitation of CO by para H_2 up to $J = 14$ were taken from Flower (2001) and scaled up by 21% to account for excitation by He. Cool gas (approximately 10 K) such as that found in cosmic-ray–heated cloud cores gives rise to substantial emission in the millimeter CO lines but does not have sufficient thermal energy to populate higher states such as $J = 6$. On the other hand, warm gas such as the few hundred K gas found in photodissociation regions (PDRs) near massive young stars will emit much more power in $J = 6$–5 than in $J = 2$–1 or $J = 1$–0 (Harris et al. 1987; Kaufman et al. 1999). Thus, we use a two-component model to explain the observed CO flux up to $J = 7$–6. In reality, we expect a continuum of temperatures and densities, but with the limited number of measurements available, a two-component model is a reasonable approximation.

The LVG model for each component takes three parameters: kinetic temperature, H_2 density, and CO column density per unit velocity. The LVG models for the two components are calculated independently, and the line intensities are summed using separate area filling factors for the two components. Calling the area filling factor Φ, H_2 density n, and CO column density N,

$$T_{\mathrm{model}} = \Phi_w f(T_w, n_w, N_w/\Delta v) + \Phi_c f(T_c, n_c, N_c/\Delta v)\ , \quad (2)$$

where the subscripts w and c represent the warm and cool components, respectively. If the clouds do not fill the beam, then $\Phi < 1$ and N is the cloud column density. In this case, the beam-averaged column density is ΦN. The beam-averaged column density is used to calculate the total molecular mass in the beam. If the clouds fill the beam, then $\Phi = 1$ and N is the beam-averaged column density rather than the cloud column density. (Note that solutions with $\Phi > 1$, which would correspond to more than one cloud along the line of sight, imply higher optical depths and so mathematically are treated as unit area filling factors with higher column densities, since the intensities no longer add linearly.)

3.3.1. *Calculating Likelihood Distributions*

Our two-component LVG model has nine free parameters: the H_2 kinetic temperatures T_{kin}, number densities $n(H_2)$, column densities $N(\mathrm{CO})$, and area filling factor Φ_A for the warm and cool components, plus the $^{12}\mathrm{CO}/^{13}\mathrm{CO}$ column density ratio. We determine these parameters from our 10 measured spectra. A single precise solution for the model would be unrealistic, since the number of free parameters is comparable to the number of measured lines, the data have significant uncertainties, and the model is a simplification of the real physical conditions in the source. It should also be noted that while some quantities physically have unique, well-defined values such as the beam-averaged column density, others do not, e.g., the kinetic temperature of the gas.

In our analysis, we assume that the measured line strengths, represented by the vector $\boldsymbol{M}$, have Gaussian-distributed random errors of known σ. The model parameters are collected into a vector $\boldsymbol{a}$, and the set of calculated antenna temperatures is denoted by $\boldsymbol{T}(\boldsymbol{a})$. If we knew the true values of the model parameters, ignoring that the model itself only approximates the true physical conditions, then the probability density for measuring a given set of line intensities $\boldsymbol{M}$ is given by

$$P(\boldsymbol{M}|\boldsymbol{a}, \boldsymbol{\sigma}) = \prod_{i=1}^{10} \frac{1}{\sqrt{2\pi}\sigma_i} \exp\left\{ -\frac{1}{2}\left[\frac{M_i - T_i(\boldsymbol{a})}{\sigma_i}\right]^2 \right\}\ . \quad (3)$$

Bayes' theorem allows us to use this probability density to compute the likelihood of a particular set of parameters $\boldsymbol{a}$ given a set of measurements $\boldsymbol{M}$. In addition, it allows other information about the parameters $\boldsymbol{a}$ to be included in the calculation through the prior likelihood function $P(\boldsymbol{a})$:

$$P(\boldsymbol{a}|\boldsymbol{M}, \boldsymbol{\sigma}) = \frac{P(\boldsymbol{a})P(\boldsymbol{M}|\boldsymbol{a}, \boldsymbol{\sigma})}{\int d\boldsymbol{a}\, P(\boldsymbol{a})P(\boldsymbol{M}|\boldsymbol{a}, \boldsymbol{\sigma})}\ . \quad (4)$$

We can integrate to compute the likelihood distribution of

TABLE 2
MEASURED M82 LINE STRENGTHS

Transition	Northeast Lobe (9, 4) [a] I (K km s^{-1})	Northeast Lobe (9, 4) [a] T (K)	Southwest Lobe (−9, −4) I (K km s^{-1})	Southwest Lobe (−9, −4) T (K)	σ [b] (%)
^{12}CO $J = 1$–0 [c]	529	2.94	620	3.88	7
^{12}CO $J = 2$–1 [d]	748	4.16	751	4.69	7
^{12}CO $J = 3$–2	523	2.91	476	2.97	8
^{12}CO $J = 4$–3	427	2.37	332	2.08	10
^{12}CO $J = 6$–5	179	0.99	224	1.40	12
^{12}CO $J = 7$–6 [c]	122	0.68	154	0.96	12
^{13}CO $J = 1$–0 [c]	37.0	0.205	54.2	0.339	8
^{13}CO $J = 2$–1 [c,e]	54.3	0.302	63.6	0.398	12
^{13}CO $J = 3$–2 [f,g]	24.9	0.138	26.0	0.163	50
^{13}CO $J = 6$–5 [h]	<4.7	<0.026	<4.7	<0.029	30 mK

NOTE.—Values correspond to a FWHP beam of 24″.4. Intensities were integrated from 25 to 395 km s^{-1}. Temperatures are averages computed as $I/\Delta v$, where $\Delta v = 180$ km s^{-1} for the northeast position and $\Delta v = 160$ km s^{-1} at the southwest position. These widths were chosen so that the temperatures would be representative of the average temperatures in the primary components of the lines. In all cases except ^{13}CO $J = 6$–5, the statistical error in integrated intensity due to channel noise is much smaller than calibration uncertainties.

[a] Offsets in arcseconds are based on a reference point halfway between the $J = 6$–5 antenna temperature peaks, corresponding to R.A. 09^{h}55^{m}51^{s}.8, decl. 69°40′47″ J2000. The northeast and southwest positions are at the $J = 6$–5 peaks, but are inside of the low-J peaks.

[b] Values are estimates based on a combination of factors, including effects related to calibration and smoothing. The real uncertainty is generally much larger than estimates based solely on the rms channel noise. These values of σ were used as inputs of the LVG modeling in § 3.3.

[c] Estimated by scaling integrated intensities published by Mao et al. 2000 based on their observations with the IRAM 30 m telescope and the HHT by 0.92 to account for our broader beam.

[d] Calculated from Plateau de Bure Interferometer data provided by Weiss et al. 2001.

[e] Mao et al. warn that because of the limited extent of their ^{13}CO $J = 2$–1 map, their values should be considered with caution.

[f] Values for a 24″.4 FWHP beam were approximated by scaling observations made with a 25″.5 beam up by 3.6%.

[g] The integrated intensities for ^{13}CO $J = 3$–2 presented here are much lower than those published elsewhere. Because of the wide range of measured values, the antenna temperatures used for LVG models in § 3.3 were 50% larger than the values in this table. The large value of σ reflects this uncertainty. More observations of this line are needed.

[h] Line was not detected after 96 minutes of integration time near the central pointing. Values correspond to 3 σ limits found by scaling σ for a 14″ beam calculated from the rms channel noise by a factor of 0.59 to approximate a 24″.4 beam. The large 1 σ value in the right-hand column reflects concerns that uncertainties involving zeroth-order baseline subtraction and a small amount of baseline ripple could dominate over the channel noise.

any one parameter,

$$P_{ai}(x) = \int d\boldsymbol{a}\, P(\boldsymbol{a}|\boldsymbol{M}, \boldsymbol{\sigma})\delta(a_i - x) \ . \tag{5}$$

We can also compute likelihood density curves for functions of the parameters, such as pressure and beam-averaged column density. The likelihood distribution of some function $x = f(\boldsymbol{a})$ is given by

$$P_f(x) = \int d\boldsymbol{a}\, P(\boldsymbol{a}|\boldsymbol{M}, \boldsymbol{\sigma})\delta(f(\boldsymbol{a}) - x) \ . \tag{6}$$

The main difficulty with this approach (and a possible source of controversy) is the choice of the prior probability density function $P(\boldsymbol{a})$. In particular, one must choose $P(\boldsymbol{a})$ even if one has no prior knowledge of the parameters $\boldsymbol{a}$. Bayes' postulate tells us to set $P(\boldsymbol{a}) = 1$ for this case, since all values of $\boldsymbol{a}$ are a priori equally likely. It should be noted, however, that even this choice introduces a bias, since choosing a different set of parameters $\boldsymbol{a}$ changes $P(\boldsymbol{a})$. For example, using Bayes' postulate with the column density as a parameter would result in a different prior probability density $P(\boldsymbol{a})$ than using the logarithm of the column density as the parameter.

The likelihood distributions are computed numerically by creating an array of bins initialized to zero for each of the physical quantities of interest. The integrands of equations (5) and (6) are calculated inside a nested loop over all parameters $\boldsymbol{a}$, and at each iteration are added to the appropriate bins of the arrays. The resulting arrays are then scaled by functions of the loop step sizes and bin widths for normalization.

3.3.2. *Constraints on Model Parameters*

We first ran a calculation with a single-component model, where the prior probability density function $P(\boldsymbol{a})$ was determined by the assumption that all values of the logarithms of the parameters are equally likely. Although the resulting likelihood curves for the parameters were reasonable, the fit to the measured data was poor. A two-component model was then calculated over a coarse grid to estimate the

cool-component kinetic temperature. The cool-component kinetic temperature was fixed at 14 K based on this result to speed up subsequent calculations. Since accurate collisional excitation rates were only available for temperatures up to 400 K, $P(\boldsymbol{a})$ was assumed to equal zero if $T_{\rm kin} > 400$ K. Since we had already found that a single-component model was a poor fit, we also set $P(\boldsymbol{a})$ to zero for models where the cool component accounted for less than 20% of the $J = 2$–1 intensity. In all cases, area filling factors were not allowed to be greater than unity, since larger area filling factors imply higher optical depths and so mathematically must be treated as unit area filling factors with higher column densities. The H_2 densities were limited to the range of 10^2–10^6 cm^{-3}.

Two unphysical situations were rejected through the use of $P(\boldsymbol{a})$. First, the total molecular mass was not allowed to be larger than the dynamical mass. Secondly, models with impossibly large column lengths were rejected. These restrictions eliminated models with very large column density and low volume density. Both restrictions require knowledge of the ^{12}CO/H_2 abundance ratio. Frerking, Langer, & Wilson (1982) measured a ratio of 8.5×10^{-5} based on observations of clouds in Taurus and ρ Ophiuchi. The ratio may be higher in warm, star-forming clouds; Lacy et al. (1994) measured a ratio of 2.7×10^{-4} in NGC 2024. Since the uncertainty of these measurements is large, and the average value in M82 may be substantially different than in local clouds, we conservatively assume that

$$^{12}\mathrm{CO}/\mathrm{H}_2 < X_{\rm max} = 5 \times 10^{-4} \ . \qquad (7)$$

The outer edges of our 24″.4 FWHP beams are about 390 pc from the dynamical center of M82. Since each beam is mostly on one side of the dynamical center, and the beam covers most of the molecular material on that half of the galaxy, we exclude solutions in which the mass in the beam is larger than one-half of the dynamical mass. Thus, we require

$$\Phi_w N_w + \Phi_c N_c < \frac{1}{2}\frac{M_{\rm dyn}}{m_{\rm H_2}}\frac{X_{\rm max}}{A_{\rm beam}} \ , \qquad (8)$$

where the subscripts w and c indicate the warm and cool components, respectively, and $m_{\rm H_2}$ is the mass of a single H_2 molecule. We take the area of the beam to be 145,000 pc^2, and, based on a rotational velocity of 135 km s^{-1} at a radius of 390 pc, we take the dynamical mass to be 1.7×10^9 $M_\odot$.

Solutions for which the length of the column is larger than the entire molecular region can clearly be excluded. If the area filling factor Φ_A is less than unity, then the maximum possible column length is smaller still. Based on simple geometrical arguments, and given that the bright part of the molecular region is about 900 pc across, we require that

$$\frac{N(\mathrm{CO})}{n(\mathrm{H}_2)X_{\rm max}} < \sqrt{\Phi_A}(900 \text{ pc}) \ . \qquad (9)$$

3.3.3. *Resulting Likelihood Distributions and Confidence Intervals*

Using a prior likelihood function $P(\boldsymbol{a}) = 0$ for the rejected regions of parameter space discussed above, and assuming that all values of the logarithms of the parameters are equally likely everywhere else, we calculated likelihood curves for all eight free parameters as well as nine derived quantities. The best-fit χ^2 of 1.9 and 1.8 for the northeast and southwest positions, respectively, each based on 10 measurements and eight free parameters, indicate that both the model and our choices of σ are reasonable. Likelihood curves of the free parameters are shown in Figure 7; the curves for derived quantities are shown in Figure 8. Median likelihood estimators and 95% confidence intervals are listed in Table 3. Note that since the values in the table were calculated from integrals over all possible solutions, the listed median values do not necessarily represent a single self-consistent solution. Example solutions are shown in Figure 9.

3.3.4. *Comparison with a Spherical-Cloud Model*

Likelihood curves were also calculated using an escape-probability function derived for spherical clouds in gravitational collapse (Goldreich & Kwan 1974). The results from the two different cloud models differ in detail but do not change the basic results of this paper; we therefore summarize the differences rather than present figures and tables of the spherical model results. The most significant difference is that the spherical cloud model predicts higher volume densities than the plane-parallel model by a factor of ~5. Column densities are a factor of ~2 larger. The kinetic temperatures are better constrained with the spherical model, with slightly lower median likelihood values. The isotopomer ratio, on the other hand, is less well constrained and a factor of ~2 higher.

A particularly interesting difference is the ratio of warm gas mass to cool gas mass. We would expect this ratio to be higher in the southwest lobe than the northeast, since the southwest lobe is brighter in most tracers of warm gas and dust, such as 12.4 μm continuum (Telesco & Gezari 1992) and CO $J = 6$–5. The likelihood distributions calculated with the plane-parallel model in Figure 8 are somewhat anomalous, since they suggest that the proportion of warm gas is higher in the northeast lobe than the southwest. The spherical model predicts a lower cool gas mass for the southwest lobe than the plane-parallel model, and leaves the cool gas mass of the northeast lobe essentially unchanged. This in turn causes the predicted ratio of warm gas mass to cool gas mass to be higher in the southwest lobe than the northeast lobe, which is more consistent with our expectations.

Not all of the determined quantities changed with the choice of escape probability function. In particular, the total beam-averaged ^{13}CO column density determinations are almost exactly the same with both spherical and plane-parallel cloud models.

3.3.5. *Discussion*

We see from Table 3 that the ^{13}CO beam-averaged column density is the most precisely determined result. This parameter is well determined not only because the ^{13}CO optical depths are lower than those of ^{12}CO, but also because the ^{12}CO measurements help constrain other physical conditions, i.e., the temperatures, densities, and filling factors. It is interesting to note that total beam-averaged column densities, which physically have unique, well-defined values, are generally more tightly constrained by the data than cloud column densities, which would be expected to cover ranges of values because of the presence of many different clouds in a single beam. After the ^{13}CO beam-averaged column density, the area filling factors and the isotopomer abundance ratio were the next most precisely determined parameters. The data only allow a lower limit to

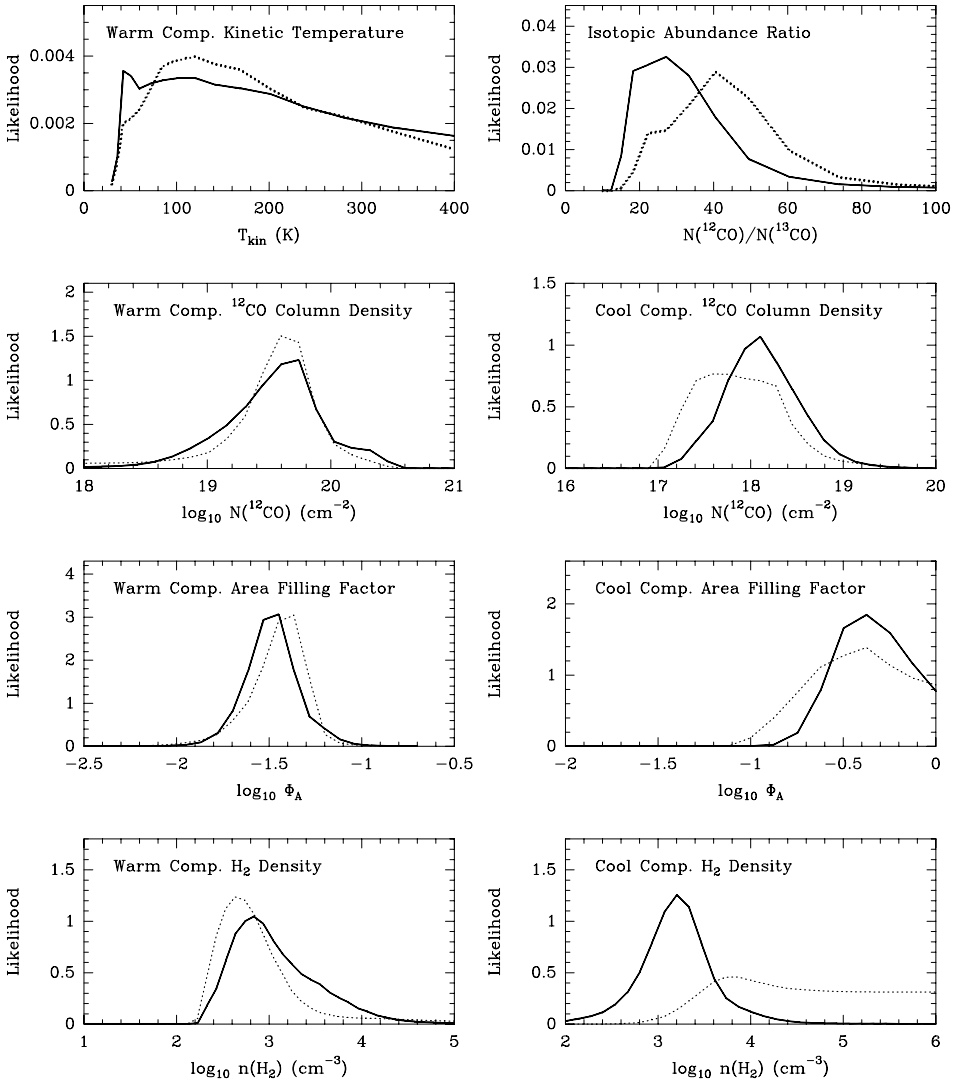

FIG. 7.—Likelihood curves of the LVG model parameters. The solid curves are for the southwest lobe, and the dotted curves the northeast lobe. The cool component temperature was fixed at 14 K. Note that all parameters are constrained except the cool component density of the northeast lobe and the warm component temperature.

be set on the cool component H_2 density and pressure in the northeast lobe. This is primarily because the level populations become thermalized in cool, dense clouds and thus are nearly independent of H_2 density. The density of the warm component is easier to constrain, since the populations of the higher J levels do not become thermalized until $n \sim 10^5$ cm^{-3}. Determinations of kinetic temperatures are biased by the nature of the two-component model. For example, the very small likelihood that the warm component is ~30 K does not mean that there is no molecular gas at 30 K in the source; rather, it means that the two-component model cannot match the measured line strengths if it assumes that all the gas in the warm component is at ~30 K. Although the model was restricted to kinetic temperatures below 400 K for purely practical reasons, it is likely that energy balance considerations would require a similar upper limit.

Figures 7 and 8 indicate that conditions in the two hot spots are very similar. These results suggest that the southwest lobe has higher beam-averaged ^{13}CO column density and lower cool-component H_2 density. The temperatures and filling factors are about the same. In both hot spots, the H_2 density is lower for the warm component than the cool. Median likelihood estimates for pressure range from $10^{4.4}$ to $10^{5.2}$ K cm^{-3}.

It is interesting to note that the median likelihood estimates of the isotopomer abundance ratio ^{12}CO/^{13}CO of 40 and 30 in the northeast and southwest lobes, respectively (Table 3) lie between the value of 25 for Galactic center clouds determined by Güsten (1989) and values ranging from 50 to 100 for M82 determined by Mao et al. (2000) and Weiss et al. (2001).

Table 4 shows typical ^{12}CO optical depths calculated from median values listed in Table 3. The warm clouds are optically thick in all transitions except J = 1–0. The cool component optical depths are of order unity for low-J transitions.

The example fits in Figure 9 show that it is necessary to understand the warm molecular component even to understand low-J CO spectra. This is because the warm component accounts for a significant fraction of the total emission even in the J = 2–1 transition. Thus, measurements of the high-J CO lines are helpful to understand not only the warm

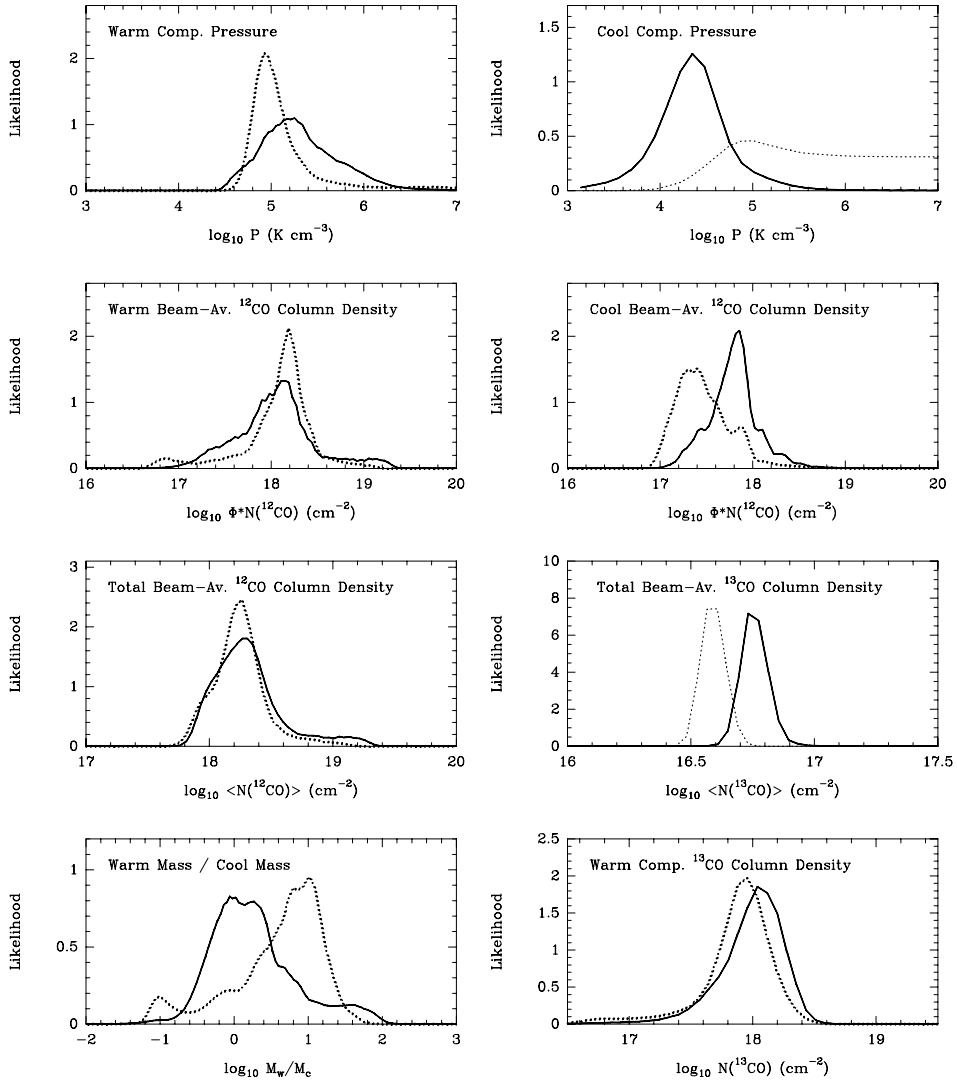

FIG. 8.—Likelihood curves for quantities derived from the LVG model parameters. The solid curves are for the southwest lobe, and the dotted curves the northeast lobe. The total average column density is the sum of the warm and cool component beam-averaged column densities.

molecular gas, but also the cool molecular component that is essentially invisible above the $J = 4$–3 line. This also explains why single-component models fail to account for the strong CO $J = 2$–1 emission relative to $J = 1$–0 and $J = 3$–2 (see, for example, Young & Scoville 1984 or Wild et al. 1992).

The total molecular mass can be estimated from the beam-averaged ^{12}CO column density. Our models found an average column density of $\langle N(\mathrm{CO})\rangle \approx 10^{18.2}$ cm^{-2} for a $J = 6$–5 integrated intensity of $I \approx 200$ K km s^{-1}. We convert the CO column density to H_2 column density by assuming a CO/H_2 abundance of $X_{\mathrm{CO}} = 10^{-4}$. Our $J = 6$–5 map has an average integrated intensity of 180 K km s^{-1} over an area of 1544 square arcseconds. Putting this together,

$$M_{\mathrm{mol}} \approx 1.6 m_{\mathrm{H_2}} \frac{\langle N(\mathrm{CO})\rangle}{X_{\mathrm{CO}}} \frac{\int\int T_A dv\, dA}{I}, \qquad (10)$$

where $m_{\mathrm{H_2}}$ is the mass of a single H_2 molecule and the factor of 1.6 accounts for the mass of helium, dust, etc. in the molecular clouds. Assuming a distance of 3.6 Mpc, $M_{\mathrm{mol}} = 1.7 \times 10^8\ M_\odot$. This value should be treated with caution, since there is no reason to expect the molecular mass to be proportional to ^{12}CO $J = 6$–5 luminosity. It is nonetheless interesting to note that this estimate is within a factor of 2 of most other published values based on low-J ^{12}CO data and rare isotopomers (Carlstrom 1988; Wild et al. 1992; Mao et al. 2000; Weiss et al. 2001).

Based on simple geometric arguments, characteristic cloud sizes can be approximated as

$$S_{\mathrm{cloud}} \approx \frac{N(\mathrm{CO})}{X_{\mathrm{CO}} n(\mathrm{H_2})}. \qquad (11)$$

If the area filling factor is close to unity, then this value should be considered an upper limit. Use of this expression gives very large sizes (tens or hundreds of pc) for warm clouds, and sizes of the order of 1 pc or smaller for cool clouds. The number of clouds in the beam of diameter D_B can estimated with

$$N_{\mathrm{clouds}} \approx X_{\mathrm{CO}}^2 D_B^2 \frac{\Phi_A n^2(\mathrm{H_2})}{N^2(\mathrm{CO})}. \qquad (12)$$

This number should be considered a lower limit if the area

TABLE 3
M82 LVG Model Results

Quantity	Northeast Lobe		Southwest Lobe	
	Range [a]	Median [b]	Range	Median
$N(^{12}CO)/N(^{13}CO)$	20–140	40	15–200	30
$\langle N(CO)\rangle$ (cm^{-2}) [c]	$10^{17.9}$–$10^{18.8}$	$10^{18.2}$	$10^{17.9}$–$10^{19.1}$	$10^{18.2}$
$\langle N(^{13}CO)\rangle$ (cm^{-2}) [c]	$10^{16.48}$–$10^{16.67}$	$10^{16.57}$	$10^{16.63}$–$10^{16.85}$	$10^{16.73}$
M_w/M_c [d]	0.09–26	5	0.24–50	1.5
Warm Component				
T_{kin} (K) [e]	>50	170	>50	170
$n(H_2)$ (cm^{-3})	$10^{2.4}$–$10^{5.0}$	$10^{2.8}$	$10^{2.4}$–$10^{4.3}$	$10^{3.0}$
$N(CO)$ (cm^{-2})	$10^{18.3}$–$10^{20.1}$	$10^{19.5}$	$10^{18.6}$–$10^{20.2}$	$10^{19.5}$
$N(^{13}CO)$ (cm^{-2})	$10^{16.9}$–$10^{18.2}$	$10^{17.9}$	$10^{17.3}$–$10^{18.3}$	$10^{18.0}$
Φ_A [f]	0.013–0.06	0.03	0.015–0.06	0.03
$\Phi_A N(CO)$ (cm^{-2}) [g]	$10^{16.9}$–$10^{18.7}$	$10^{18.1}$	$10^{17.2}$–$10^{19.1}$	$10^{18.0}$
$T_{kin}n(H_2)$ (K cm^{-3}) [h]	$10^{4.7}$–$10^{7.0}$	$10^{5.0}$	$10^{4.6}$–$10^{6.2}$	$10^{5.2}$
Cool Component				
T_{kin} (K)	...	14	...	14
$n(H_2)$ (cm^{-3})	$>10^{3.3}$	$10^{3.8}$	$10^{2.5}$–$10^{4.2}$	$10^{3.3}$
$N(CO)$ (cm^{-2})	$10^{17.1}$–$10^{18.8}$	$10^{17.8}$	$10^{17.3}$–$10^{18.9}$	$10^{18.0}$
$N(^{13}CO)$ (cm^{-2})	$10^{15.2}$–$10^{17.0}$	$10^{16.2}$	$10^{15.2}$–$10^{17.1}$	$10^{16.7}$
Φ_A [f]	0.12–1	0.34	0.2–1	0.4
$\Phi_A N(CO)$ (cm^{-2}) [g]	$10^{17.0}$–$10^{18.1}$	$10^{17.4}$	$10^{17.2}$–$10^{18.3}$	$10^{17.8}$
$T_{kin}n(H_2)$ (K cm^{-3}) [h]	$>10^{4.4}$	$10^{4.9}$	$10^{3.6}$–$10^{5.3}$	$10^{4.4}$

Note.—Model is constrained with eightfree parameters fitted to the 10 measured line temperatures listed in Table 2. The parameters are T_{kin}, $n(H_2)$, $N(CO)$, and Φ_A for the warm and cool components, plus the $N(^{12}CO)/N(^{13}CO)$ ratio. The cool component temperature was fixed at 14 K. Assumed velocity widths are 180 km s^{-1} for the northeast position and 160 km s^{-1} for the southwest position.

[a] Ranges are for 95% confidence intervals.

[b] Median likelihood values do not represent a single self-consistent solution. See § 3.3.1 for an explanation of how they were calculated.

[c] Beam-averaged column density including both warm and cool components.

[d] Warm gas to cool gas mass ratio.

[e] An upper temperature limit of 400 K is set by the range of available collision rates. Otherwise, the model results do not exclude higher temperatures for the warm gas.

[f] Area filling factor.

[g] Beam-averaged column density.

[h] Pressure.

filling factor is close to unity. We see from this expression that the number of warm clouds is small, perhaps a few, while the number of cool clouds is quite large. Our model results therefore suggest that the nucleus of M82 is a region containing a large number of small, cool clouds, and a small number of large, low-density warm clouds. The interferometer map in Figure 5, with a 1″.5 × 1″.4 beam size corresponding to about 25 pc, shows clumpiness at size scales consistent with these predictions. It should be noted, however, that the uncertainty of equation (12) is very large, since it involves products and quotients of many quantities of significant uncertainty.

TABLE 4
^{12}CO Optical Depths in M82

J	Northeast Lobe		Southwest Lobe	
	τ_{warm}	τ_{cool}	τ_{warm}	τ_{cool}
1–0	0.9	0.4	0.7	0.9
2–1	3.4	0.9	2.8	1.9
3–2	6.7	0.7	5.6	1.3
4–3	9.8	0.2	8.4	0.2
5–4	11.5	0.02	10.4	0.01
6–5	10.7	1×10^{-3}	10.9	4×10^{-4}
7–6	7.1	5×10^{-5}	9.0	2×10^{-5}

Note.—Optical depths were computed in the LVG approximation from the median likelihood values listed in Table 3.

If the warm component in each lobe were a single spherical cloud, then for an area filling factor of $\Phi_A = 0.03$ in a 24″.4 diameter beam, the cloud diameter is 4″, or $\phi_{cloud} \approx 75$ pc. Assuming that ^{13}CO column density and visual extinction are related by $N(^{13}CO) = 2 \times 10^{15} A_v$ cm^{-2} (Dickman 1978; Frerking, Langer, & Wilson 1982), then for $N(^{13}CO) = 10^{18}$ cm^{-2}, the warm-cloud visual extinction is $A_v \approx 500$. Thus, to keep this gas warm, the cloud must be a star-forming zone with stars scattered throughout the region.

The cool cloud ^{13}CO column density is around $10^{16.5}$ cm^{-2}. Using the same conversion factor between ^{13}CO column density and visual extinction as above, the cool-cloud visual extinction is around $A_v \approx 16$, which is sufficient to shield the cloud from warming stellar radiation.

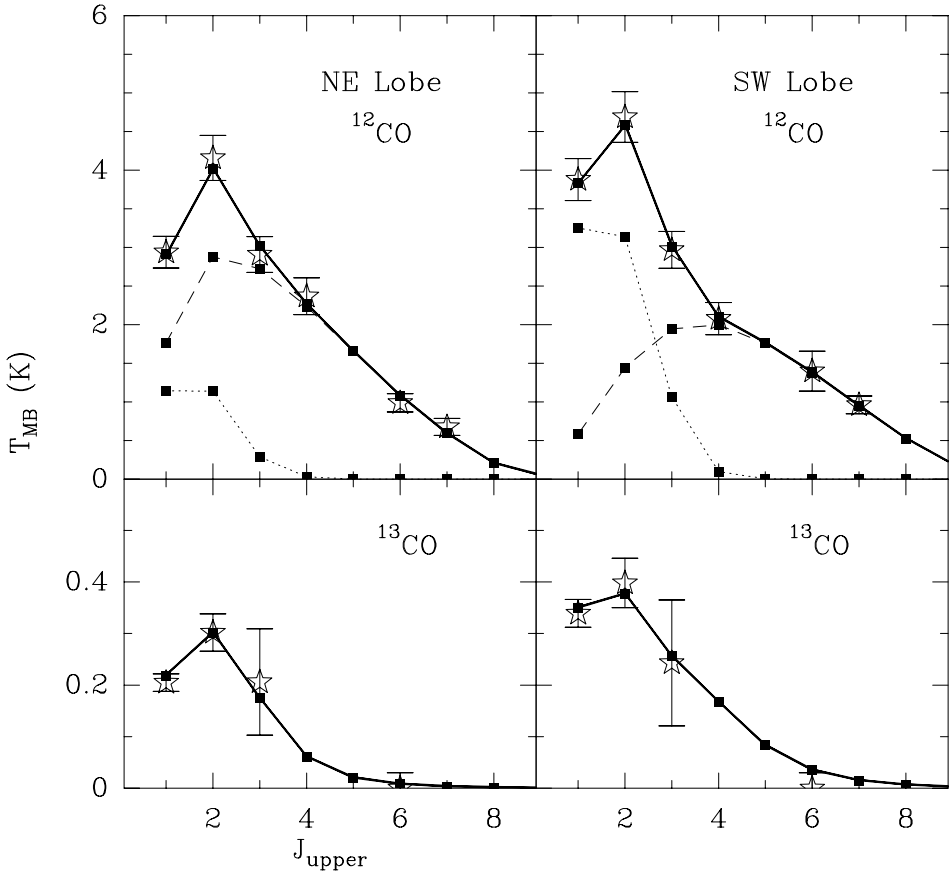

FIG. 9.—Measured temperatures with example LVG solutions for the two main hot spots in M82. Measured values (indicated with stars) and 1 σ error bars are taken from Table 2, except for ^{13}CO $J = 3$–2, which was scaled up by 50% as explained in the table notes. The cool and warm components are shown by dotted and dashed lines, respectively, and total temperatures by a solid line. The solution for the northeast lobe is an example solution with low warm component H_2 density; in this case, $10^{2.6}$ cm^{-3}. For this solution, the pressures of the two components are both around 10^5 K cm^{-3}, and the warm component cloud sizes are large, ~200 pc. The southwest lobe example, on the other hand, has a warm component H_2 density of $10^{3.3}$ cm^{-3} and cloud size around 20 pc.

The 24″.4 beam-averaged visual extinction including both warm and cool components calculated from $\langle N(^{13}\mathrm{CO})\rangle = 10^{16.7}$ is $\langle A_v\rangle \approx 25$. This is comparable to the range of $A_v = 17$–50 for a 27″ beam based on an isothermal graybody fit to 40 μm–3.3 mm continuum (Hughes et al. 1994). It should be noted that the continuum measurement should be sensitive to atomic gas not seen in the CO data. The beam-averaged H_2 column density can also be calculated from the ^{13}CO column density; assuming $N(\mathrm{H_2}) = 5 \times 10^5\, N(^{13}\mathrm{CO})$ (Dickman 1978), we find $\langle N(\mathrm{H_2})\rangle = 10^{22.1}$.

In part because of the nature of the model and the somewhat arbitrary distinction between "warm" and "cool" gas, the ratio of warm gas mass to cool gas mass is not well constrained. It is nonetheless interesting to note that the mass ratio likelihood distribution shown in Figure 8 and the warm component kinetic temperature shown in Figure 7 together suggest that over half of the molecular gas mass is warmer than the graybody dust temperature of 48 K measured with the *Infrared Space Observatory* (*ISO*) and the James Clerk Maxwell Telescope (JCMT; Colbert et al. 1999; Hughes et al. 1994). Detecting ^{13}CO in $J = 4$–3 and $J = 6$–5 would help constrain this mass ratio, since column densities for the warm component could be more accurately determined at the lower optical depths of this species than with ^{12}CO.

Comparing the $J = 6$–5/$J = 2$–1 line ratio map in Figure 6 to the measured intensities in Table 2, we see that the peak ratio at the hot spots is substantially higher than the 24″.4 values of 0.24 and 0.30 used in the LVG models for the northeast and southwest hot spots, respectively. This is largely an effect of beam filling factor. The temperature, density, and pressure may also be higher near the peak than indicated by the 24″.4 beam data.

4. CONCLUSIONS

A two-component LVG model of the molecular gas in M82 is consistent with the measured ^{12}CO and ^{13}CO spectra up to $J = 7$–6, and matches the large observed $J = 2$–1/$J = 1$–0 and $J = 2$–1/$J = 3$–2 ratios. Results of this model suggest that the nuclear region contains a large number of small, cool molecular clouds, and a small number of large, warm, low-density clouds.

We have demonstrated an approach to the evaluation of excitation models that provides important insight into how well the model parameters and various quantities derived from them are constrained by the measured data. This is accomplished by computing a likelihood density curve for each of the parameters and derived quantities. We have also demonstrated how prior knowledge and/or physical constraints can be incorporated into this evaluation. We find

that a range of conditions is consistent with the measured M82 data. This is to be expected for a complicated region like a galactic nucleus; simple excitation models cannot be expected to determine precise results. On the other hand, simple models can be used to exclude large regions of parameter space.

The results of this analysis show that the most precisely determined quantity is the ^{13}CO beam-averaged column density, with a value of about 4.5×10^{16} cm^{-2} in both lobes. The beam-averaged column density of ^{12}CO was determined to within a factor of a few to be $10^{18.2}$ cm^{-2} in both lobes. The area filling factors were found to be near unity for the cool molecular gas, and around 0.03 for the warm molecular gas.

Median likelihood estimates of the isotopomer abundance ratio ^{12}CO/^{13}CO in the northeast and southwest lobes of M82 are 40 and 30, respectively. These estimates lie between the value of 25 for Galactic center clouds determined by Güsten (1989) and values ranging from 50 to 100 for M82 determined by Mao et al. (2000) and Weiss et al. (2001).

Although the temperature of the warm molecular gas in the nucleus of M82 was not well constrained (no upper limit to the temperature was found), it is likely that over half of the total molecular mass is warmer than measured dust temperatures of 48 K.

The density of warm molecular gas in the nuclear region of M82 is low, with median likelihood estimates around 10^3 cm^{-3}. Cool molecular gas appears to be typically more dense than warm molecular gas. Median likelihood estimates for the warm gas and cool gas pressures in the two lobes range from $10^{4.4}$ to $10^{5.2}$ K cm^{-3}.

The ^{12}CO $J = 6$–5 to ^{12}CO $J = 2$–1 line ratio is at least 5 times larger in the southwest lobe of M82 than in the Galactic center, indicating that the proportion of molecular gas that is warm is significantly larger in the nuclear region of M82 than in the Galactic center.

We would like to thank A. Weiss, N. Neininger, S. Hüttemeister, and U. Klein for providing access to their Plateau de Bure Interferometer data cubes. This research was supported in part by the NSF CSO grant AST 99-80846. The development of the SIS mixers and HEMT amplifiers was supported in part by grants from NASA (NAG5-4890, NAG5-9493) and the NASA/USRA SOFIA instrument program (grant 8500-98-011). The SIS devices used were produced at JPL's Center for Space Microelectronics Technology. Spectrometer development was supported by the NSF grant AST 98-19747.

APPENDIX

RATIO MAP CALCULATION

A straightforward approach to computing a ratio between two maps is to smooth the higher resolution map to the resolution of the lower, and divide integrated intensities directly. This technique has three drawbacks. First, it throws away the line profile information, which from inspection of Figure 1 can be seen to contain information about position. Second, smoothing throws away spatial information. Finally, noise causes the error in division to become large as the signal levels decrease.

We have employed a calculus of variations approach to compute a line ratio map that uses all available information, and is well behaved as the signal-to-noise ratio decreases away from bright centers. Furthermore, with this method, a Lagrange multiplier provides a natural way to adjust the resolution of the resulting ratio map. This method is similar to the linear regularization methods described by Press et al. (1992).

In general, we expect any region of a galaxy with ^{12}CO $J = 6$–5 emission to also emit in ^{12}CO $J = 2$–1. Furthermore, the spectral line profiles at any given location in a galaxy in the two transitions are likely to be similar if observed at high spatial resolution. Therefore, we assume that the measured $J = 6$–5 emission can be modeled as the interferometric $J = 2$–1 data times a line ratio map, convolved to the resolution of the measured $J = 6$–5 data,

$$T_{6-5}(\boldsymbol{r}, v) = \int G(\boldsymbol{r} - \boldsymbol{r}') T_{2-1}(\boldsymbol{r}', v) \rho(\boldsymbol{r}')\, d\boldsymbol{r}' \ , \tag{A1}$$

where $\boldsymbol{r}$ is the mapping offset, $G(\boldsymbol{r} - \boldsymbol{r}')$ is the smoothing kernel which convolves the $J = 2$–1 beam to the $J = 6$–5 beam, $\rho(\boldsymbol{r})$ is the unknown ratio map, and v is the velocity.

All spectra are resampled so that the velocity channels are the same for both maps. The positions observed, on the other hand, will typically be different. Since the data are discrete, we define matrix F as follows:

$$F_{ij} \equiv G(\boldsymbol{r}_i - \boldsymbol{r}'_j) T_{2-1}(\boldsymbol{r}'_j, v_i)/\sigma(\boldsymbol{r}_i, v_i) \ , \tag{A2}$$

where the index i represents a velocity channel at a particular mapping offset $(\boldsymbol{r}_i, v_i)$ in the $J = 6$–5 data, j represents a spatial position $\boldsymbol{r}'_j$ in the $J = 2$–1 map, and with $\sigma(\boldsymbol{r}_i, v_i)$ defined as the standard deviation of the channel $(\boldsymbol{r}_i, v_i)$ in the $J = 6$–5 data.

The ratio map $\rho(\boldsymbol{r})$ is written as a vector $\boldsymbol{\rho}$, where each element ρ_j represents the line ratio at offset $\boldsymbol{r}_j$ in the map. The ratio map is sampled on the same coordinate grid as the ^{12}CO $J = 2$–1 map. The $J = 6$–5 map is represented as a vector $\boldsymbol{t}$, where t_i is the σ-normalized antenna temperature of channel i,

$$t_i = T_{6-5}(\boldsymbol{r}_i, v_i)/\sigma(\boldsymbol{r}_i, v_i) \ . \tag{A3}$$

With these definitions, we can now calculate the σ-normalized χ^2,

$$\chi^2 \equiv (F\boldsymbol{\rho} - \boldsymbol{t})^2 \ . \tag{A4}$$

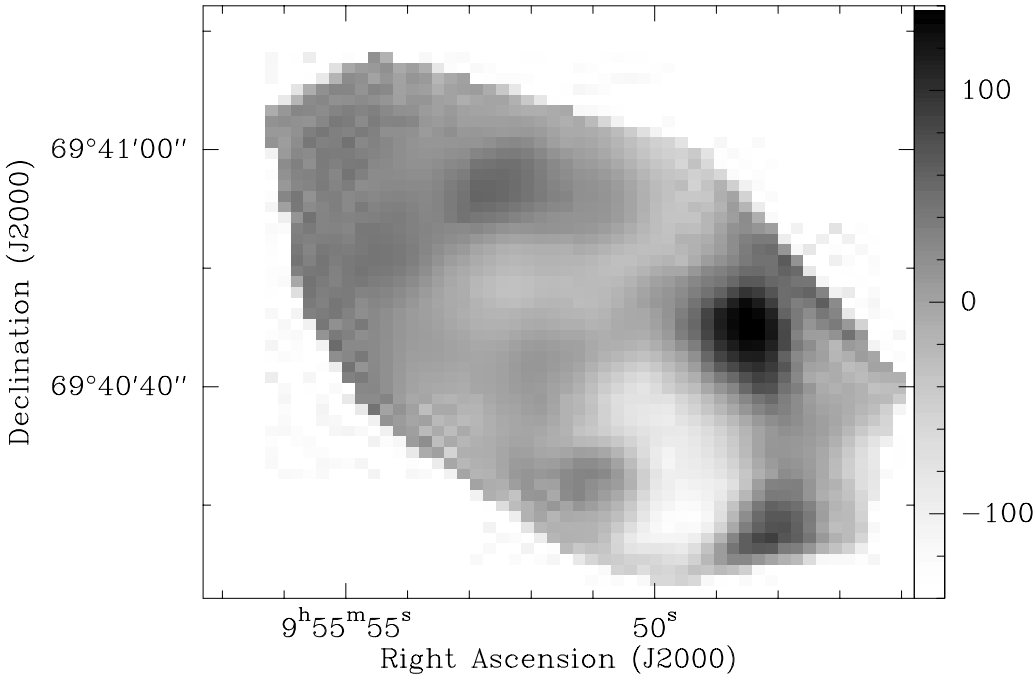

FIG. 10.—Residuals of the ^{12}CO $J = 6$–$5/J = 2$–1 line ratio map in K km s^{-1}. The larger errors in the southwest end of the galaxy may be due to a small pointing drift during the observations.

If $\boldsymbol{\rho}$ is adjusted to minimize χ^2, the resulting ratio map will tend to track the noise in the $J = 6$–5 map. To avoid this undesirable behavior, we define a function that is minimized when $\boldsymbol{\rho}$ is smooth. The integral of the square of the gradient of $\rho(\boldsymbol{r})$ has this property. We define

$$S \equiv \int |\nabla \rho(\boldsymbol{r})|^2 \, d\boldsymbol{r} \, . \tag{A5}$$

In the discrete case, a symmetric nonnegative-definite matrix D can be found such that

$$S = \boldsymbol{\rho} D \boldsymbol{\rho} \, . \tag{A6}$$

We introduce a Lagrange multiplier, λ, and solve $\delta(\chi^2 + \lambda S) = 0$ to minimize S for a constant χ^2. This expression reduces to

$$\left(F^T F + \lambda D\right)\boldsymbol{\rho} = F^T \boldsymbol{t} \, . \tag{A7}$$

For $\lambda > 0$, $F^T F + \lambda D$ is symmetric and positive definite, and therefore nonsingular. Thus, there exists a unique solution for $\boldsymbol{\rho}(\lambda)$.

Large values of λ will weight the smoothness function S more heavily in the minimization, resulting in a smoother ratio map and a higher χ^2. Small λ will result in a lower χ^2 but a noisier ratio map. Thus, the parameter λ can be adjusted to obtain a suitable trade-off between spatial resolution and noise. Note that large values of λ introduce the systematic effect of forcing the entire ratio map to a constant value. If the signal-to-noise ratio of the data is sufficiently high and the smoothing kernel G is well known, λ can be made small enough that the ratio map will approach the resolution of the denominator map. Thus, this technique is a deconvolution, since the ratio map can be at a higher resolution than the numerator map.

We computed ratio maps for a variety of values of λ, and selected Figure 6 based primarily on visual inspection. To aid this selection, we also calculated residuals by finding the difference between the measured $J = 6$–5 data and $T_{6\text{–}5}(\boldsymbol{r}, v)$ computed in equation (A1). The rms residual per channel of the fit shown in Figure 6 is 0.34 K. The integrated intensity of the residuals are shown in Figure 10.

REFERENCES

Brouillet, N., & Schilke, P. 1993, A&A, 277, 381
Carlstrom, J. 1988, Ph.D. thesis, Univ. California at Berkeley
Colbert, J. W., et al. 1999, ApJ, 511, 721
Dickman, R. L. 1978, ApJS, 37, 407
Fixsen, D. J., Bennett, C. L., & Mather, J. C. 1999, ApJ, 526, 207
Flower, D. R. 2001, J. Phys. B, 34, 2731
Freedman, W. L., et al. 1994, ApJ, 427, 628
Frerking, M. A., Langer, W. D., & Wilson, R. W. 1982, ApJ, 262, 590
Goldreich, P., & Kwan, J. 1974, ApJ, 189, 441
Güsten, R. 1989, in The Center of the Galaxy, ed. M. Morris (Dordrecht: Kluwer), 89
Harris, A. I., Hills, R. E., Stutzki, J., Graf, U. U., Russell, A. P. G., & Genzel, R. 1991, ApJ, 382, L75
Harris, A. I., Stutzki, J., Genzel, R., Lugten, J. B., Stacey, G. J., & Jaffe, D. T. 1987, ApJ, 322, L49
Harris, A. I., & Zmuidzinas, J. 2001, Rev. Sci. Instrum., 72, 1531
Hughes, D. H., Gear, W. K., & Robson, E. I. 1994, MNRAS, 270, 641
Kaufman, M. J., Wolfire, M. G., Hollenbach, D. J., & Luhman, M. L. 1999, ApJ, 527, 795
Lacy, J. H., Knacke, R., Geballe, T. R., & Tokunaga, A. T. 1994, ApJ, 428, L69

Lord, S. D., Hollenbach, D. J., Haas, M. R., Rubin, R. H., Colgan, S. W. J., & Erickson, E. F. 1996, ApJ, 465, 703
Mao, R. Q., Henkel, C., Schulz, A., Zielinsky, M., Mauersberger, R., Störzer, H., Wilson, T. L., & Gensheimer, P. 2000, A&A, 358, 433
Neininger, N., Guélin, M., Klein, U., García-Burillo, S., & Wielebinski, R. 1998, A&A, 339, 737
Pierce-Price, D., et al. 2000, ApJ, 545, L121
Press, W. H., Teukolsky, S. A., Vetterling, W. T., & Flannery, B. P. 1992, Numerical Recipes in C (2d ed.; New York: Cambridge Univ. Press)
Scoville, N. Z., & Solomon, P. M. 1974, ApJ, 187, L67
Telesco, C. M., & Gezari, D. Y. 1992, ApJ, 395, 461
Ward, J., Miller, D., Zmuidzinas, J., O'Brien, P., LeDuc, H. G., & Bicknell-Tassius, R. 2000, Proc. 11th Int. Symp. Space Terahertz Technology (Pasadena: JPL), 570
Weiss, A., Neininger, N., Hüttemeister, S., & Klein, U. 2001, A&A, 365, 571
Wild, W., Harris, A. I., Eckart, A., Genzel, R., Graf, U. U., Jackson, J. M., Russell, A. P. G., & Stutzki, J. 1992, A&A, 265, 447
Young, J. S., & Scoville, N. Z. 1984, ApJ, 287, 153
Yun, M. S., Ho, P. T., & Lo, K. Y. 1993, ApJ, 411, L17